

# Mn incorporation in as-grown and annealed (Ga,Mn)As layers studied by x-ray diffraction and standing-wave fluorescence

V. Holý,<sup>1</sup> Z. Matěj,<sup>1</sup> O. Pachrová,<sup>2</sup> V. Novák,<sup>2</sup> M. Cukr,<sup>2</sup> K. Olejník,<sup>2</sup> and T. Jungwirth<sup>2,3</sup>

<sup>1</sup>*Charles University, Faculty of Mathematics and Physics,*

*Department of Electronic Structures, Ke Karlovu 5, 121 16 Prague 2, Czech Republic*

<sup>2</sup>*Institute of Physics ASCR, Cukrovarnická 10, 162 53 Praha 6, Czech Republic*

<sup>3</sup>*School of Physics and Astronomy, University of Nottingham, Nottingham NG7 2RD, UK*

(Dated: February 6, 2008)

A combination of high-resolution x-ray diffraction and a new technique of x-ray standing wave fluorescence at grazing incidence is employed to study the structure of (Ga,Mn)As diluted magnetic semiconductor and its changes during post-growth annealing steps. We find that the film is formed by a uniform, single crystallographic phase epilayer covered by a thin surface layer with enhanced Mn concentration due to Mn atoms at random non-crystallographic positions. In the epilayer, Mn incorporated at interstitial position has a dominant effect on lattice expansion as compared to substitutional Mn. The expansion coefficient of interstitial Mn estimated from our data is consistent with theory predictions. The concentration of interstitial Mn and the corresponding lattice expansion of the epilayer are reduced by annealing, accompanied by an increase of the density of randomly distributed Mn atoms in the disordered surface layer. Substitutional Mn atoms remain stable during the low-temperature annealing.

PACS numbers: 61.10.Nz;68.49.Uv;75.50.Pp

## I. INTRODUCTION

Mn is incorporated in ferromagnetic (Ga,Mn)As semiconductors in substitutional  $\text{Mn}_{\text{Ga}}$  positions and fraction of Mn atoms can also occupy interstitial sites surrounded by four Ga ( $\text{Mn}_i^{(1)}$ ) or four As ( $\text{Mn}_i^{(2)}$ ) nearest neighbors, as illustrated in Fig. 1. Substitutional  $\text{Mn}_{\text{Ga}}$  ions provide local magnetic moments and holes that mediate long-range ferromagnetic coupling between the local moments.<sup>1,2</sup> The less energetically favorable  $\text{Mn}_i$  donors<sup>3,4</sup> occur due to the tendency to self-compensation in the highly Mn-doped GaAs host with nearly covalent crystal bonding.  $\text{Mn}_i$  impurities are detrimental to ferromagnetism since they act as charge and moment compensating defects.<sup>5,6,7,8,9</sup>

The concentration of  $\text{Mn}_i$  in (Ga,Mn)As epilayers can be significantly reduced by low-temperature ( $\sim 200^\circ\text{C}$ ) post-growth annealing which leads to a dramatic improvement of ferromagnetic properties of the epilayers.<sup>3,10,11,12,13</sup> For example, in the material with 9% nominal Mn doping which holds current record Curie temperature, the paramagnetic-to-ferromagnetic transition was moved from 95 K in the as-grown material up to 173 K after annealing.<sup>8</sup> Detailed analysis of Mn incorporation in (Ga,Mn)As and of the process of  $\text{Mn}_i$  removal by annealing has therefore been one of the key topics in materials research of these dilute moment ferromagnetic semiconductors.

Direct experimental evidence for the presence of interstitial Mn impurities in as-grown (Ga,Mn)As epilayers and for their reduced density after post-growth annealing was given by combined channeling Rutherford backscattering and particle induced x-ray emission measurements.<sup>3</sup> The technique can distinguish between  $\text{Mn}_i$  and  $\text{Mn}_{\text{Ga}}$  by counting the relative number of ex-

posed Mn atoms and the ones shadowed by lattice site host atoms at different channeling angles. Mn incorporation at different crystallographic positions was also studied by x-ray absorption<sup>14</sup>, and by high-resolution diffraction and structure factor measurements.<sup>15,16</sup> The extraction of partial concentrations of different types of Mn impurities in the lattice by these techniques is less straightforward as the data are sensitive not only to the crystallographic positions of Mn but also to local lattice distortions on neighboring sites. X-ray diffraction measurement of the (Ga,Mn)As epilayer lattice parameter is another indirect technique that has been used to monitor the decrease of  $\text{Mn}_i$  concentration in the epilayer after annealing.<sup>17,18,19</sup> Here the interpretation has relied on the assumption that  $\text{Mn}_i$  are the only mobile impurities during the annealing process,<sup>6,20,21</sup> and used<sup>17</sup> theoretical values<sup>22</sup> for the defect expansion coefficients in (Ga,Mn)As or assumed<sup>19</sup> specific scenarios for charge compensation that fulfill the overall charge neutrality condition.

A series of experimental works, including resistance monitored annealing combined with Auger spectroscopy,<sup>7</sup> depth-profiling by x-ray reflectometry,<sup>23</sup> and surface capping experiments,<sup>13,24,25,26</sup> have focused on the mechanism causing the decrease of  $\text{Mn}_i$  concentration in annealed (Ga,Mn)As epilayers. The studies suggest that  $\text{Mn}_i$  impurities outdiffuse to the layer surface and are passivated by oxygen when annealed in air or by forming MnAs in case of (Ga,Mn)As films overgrown by As capping layers.

In this paper we report on high resolution x-ray diffraction<sup>27</sup> (XRD) experiments and measurements of x-ray standing wave<sup>28</sup> (XSW) fluorescence at grazing incidence in as-grown and annealed (Ga,Mn)As films. The former technique allows us to monitor changes in the

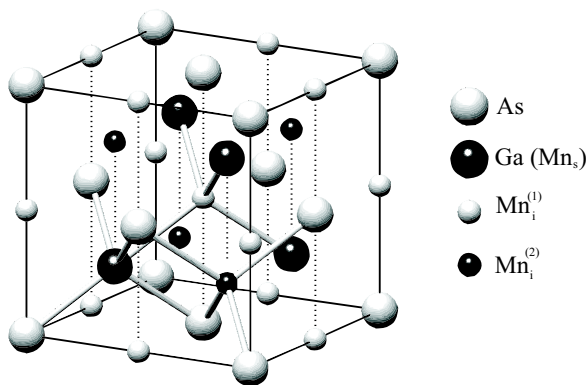


FIG. 1: The elementary unit cell of GaAs with possible positions of Mn atoms. The interstitial atoms  $\text{Mn}_i^{(2)}$  have the same lateral coordinates as the substitutional Mn atoms.

abundance of different types of impurities in the ordered part of the epilayer during annealing steps by determining individual contributions from the impurities to the lattice parameter. XSW at grazing incidence is a new experimental technique which we developed for detecting lattice-site resolved Mn fluorescence from pseudomorphic (Ga,Mn)As thin films. By small variations in the incidence angle of the primary beam we can tune the exposure from covering the entire epilayer to only a few nanometer thin surface layer. Data collected by the two complementary techniques are interpreted directly with no *a priori* assumptions on the behavior of Mn in as-grown systems and during annealing. They are used to determine crystal phases in the (Ga,Mn)As layers, to compare lattice expansion contributions from  $\text{Mn}_{\text{Ga}}$  and  $\text{Mn}_i$ , to give an estimate for the  $\text{Mn}_i$  lattice expansion coefficient, to compare stabilities of  $\text{Mn}_{\text{Ga}}$  and  $\text{Mn}_i$  atoms during annealing, and to directly monitor  $\text{Mn}_i$  outdiffusion from the (Ga,Mn)As epilayer to the surface and to characterize the surface Mn incorporation.

The paper is organized as follows. In Section II we briefly introduce the sample growth and characterization and experimental set-ups. Because of the novelty of the grazing incidence XSW technique we derive in Section III expressions for the fluorescence intensity in this geometry and show typical numerical spectra used for fitting the experimental data. Results of XSW and XRD measurements and their comparison with theory are presented in Section IV. In section V we discuss our results in the context of previous and potential future measurements, and we conclude in Section VI with a brief summary of our main findings.

## II. EXPERIMENT

Four samples were studied from a wafer grown by molecular-beam epitaxy (MBE) on a (001) GaAs semi-insulating substrate. The MBE deposition started with a 320 nm thick high-temperature GaAs buffer followed

by a 5 nm low-temperature GaAs layer and, finally, a low-temperature (Ga,Mn)As epilayer was grown with a nominal thickness of 100 nm. The substrate temperature during the low-temperature deposition was 240°C as measured by a floating thermocouple. Mn doping of  $3.5 \pm 0.5\%$  was estimated from the ratio of the growth rates measured by the RHEED oscillations before and after opening the Mn cell. The as-grown structure (sample #1) shows metallic conductivity with the room temperature conductivity of  $300 \Omega^{-1}\text{cm}^{-1}$ . The Curie temperature of 55 K was determined by SQUID magnetization measurements. Samples #2, #3, and #4 were annealed in air at 200°C for 1, 2, and 4 hours, respectively. Corresponding Curie temperatures are 65 K, 68 K, and 72 K.

Room temperature XRD measurements of the thickness of (Ga,Mn)As epilayers and of the contributions to the lattice parameter from different types of impurities were performed for coplanar symmetric 002 and 004 diffractions. We used a commercial high-resolution diffractometer equipped with conventional  $\text{CuK}\alpha$  x-ray tube, parabolic x-ray mirror, Bartels-type 4x220 Ge monochromator, and 3x220 Ge analyzing crystal.

XSW fluorescence experiments were carried out on the ID32 beamline at the European Synchrotron Radiation Facility in Grenoble, using the energy of the primary x-ray beam of 10 keV. The technique is based on the interference of the primary x-ray beam with the diffracted beam which creates a standing wave in the diffracting crystal volume. The period of the standing-wave pattern equals the distance of the diffracting net planes and the position of the antinodes of the standing wave can be sensitively tuned by changing the direction of the primary beam.<sup>28,29</sup> The presence of Mn atoms in different lattice positions was detected by measuring the fluorescent  $\text{MnK}\alpha$  radiation. The solid-state detector was placed close to the sample surface, collecting the fluorescence signal from a wide solid angle, yet avoiding direct illumination of the detector by the primary and diffracted beams.

The XSW experimental set-up is schematically illustrated in Fig. 2. For in-plane 400, 220, 200, and 420 diffractions, and for various incidence angles  $\alpha_i$  near the critical angle  $\alpha_c$  of total external reflection, we measured the dependence of the fluorescence signal  $\Phi$  on the azimuthal deviation  $\delta\eta_i$  of the primary x-ray beam from the diffraction position. Recall that (Ga,Mn)As epitaxial layers grown on GaAs buffer have a pseudomorphic structure, i.e., their in-plane lattice parameter is the same as in the substrate, however, their vertical lattice parameters are different. Therefore, the XSW experiment has to be carried out in the grazing incidence ( $\alpha_i \sim \alpha_c$ ) geometry. In this arrangement the diffracting net planes and the antinode planes of the standing wave are perpendicular to the surface allowing only for the determination of the in-plane coordinates of Mn atoms.

To our knowledge this technique has not yet been employed and we, therefore, included the following theory section which details the procedures for analyzing grazing

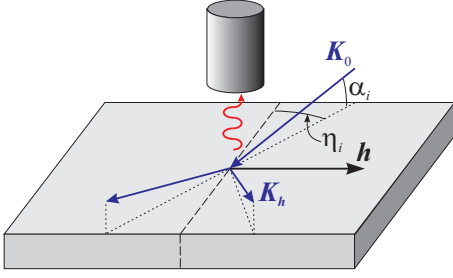


FIG. 2: Sketch of the grazing-incidence geometry. The wavy line is the fluorescence radiation, the dashed line denotes the diffracting crystallographic plane perpendicular to the sample surface.

incidence XSW data.

### III. THEORY

In the calculation of the fluorescence intensity we assume that the intensity of the fluorescence radiation emitted from a given atom is proportional to the magnitude of the Poynting vector

$$\mathbf{S} = \frac{1}{2} \text{Re}(\mathbf{E} \times \mathbf{H}^*) \quad (1)$$

of the wave field inside the (Ga,Mn)As layer in the position of a given Mn atom. For the calculation of the electric and magnetic intensities  $\mathbf{E}$  and  $\mathbf{H}$  we use the two-beam approximation of dynamical diffraction theory.<sup>30</sup> In this approximation, the wave-field inside the layer can be written as a superposition of four transmitted waves ( $\mathbf{E}_{0n}$ ,  $n = 1, \dots, 4$ ) and four diffracted waves ( $\mathbf{E}_{\mathbf{h}n} \equiv c_n \mathbf{E}_{0n}$ ,  $n = 1, \dots, 4$ ) with wave vectors  $\mathbf{k}_{0n}$  and  $\mathbf{k}_{\mathbf{h}n} = \mathbf{k}_{0n} + \mathbf{h}$ , respectively;  $\mathbf{h}$  is the diffraction vector which is assumed to be parallel to the surface. In the following, we restrict our discussion to S-polarization in which the  $\mathbf{E}$ -waves are nearly perpendicular to the sample surface.

Using the Maxwell equation

$$\mathbf{H} = \frac{1}{\omega \mu_0} \text{rot} \mathbf{E}$$

( $\mu_0$  is the vacuum permeability,  $\omega$  is the frequency of the primary x-ray radiation) we obtain the following expression for the Poynting vector

$$\mathbf{S} = S_0 \mathbf{t}_0 + S_{\mathbf{h}} \mathbf{t}_{\mathbf{h}}, \quad (2)$$

where  $\mathbf{t}_{0,\mathbf{h}}$  are the unit vectors parallel to the in-plane components of the wave vectors of the primary and

diffracted waves, respectively, and

$$S_0(\phi, Z) = \frac{K}{2\mu_0\omega} \text{Re} \left[ \sum_{n,m=1}^4 e^{iZ(k_{0nz} - k_{0mz}^*)} E_{0n} E_{0m}^* (1 + c_n e^{i\phi}) \right]$$

$$S_{\mathbf{h}}(\phi, Z) = \frac{K}{2\mu_0\omega} \text{Re} \left[ \sum_{n,m=1}^4 e^{iZ(k_{0nz} - k_{0mz}^*)} E_{0n} E_{0m}^* c_m^* (1 + c_n e^{-i\phi}) \right] \quad (3)$$

are the components of the Poynting vector parallel to the primary and diffracted beams, respectively. Since the amplitudes  $E_{0n}$  and  $E_{\mathbf{h}n}$  depend on the depth  $Z$  of the Mn atom below the surface, the entire Poynting vector depends on  $Z$  as well. In Eqs. (3),  $\phi = \mathbf{h} \cdot \mathbf{r}$ , where  $\mathbf{r}$  is the position of the Mn atom within the GaAs unit cell. Parameters  $E_{0n}$ ,  $c_n$ , and  $k_{0nz}$  were calculated from the two-beam dynamical diffraction theory taking into account four tie-points on the dispersion surface.<sup>27,30</sup>

The fluorescence signal is proportional to the weighted sum of the contributions of all Mn atoms

$$\Phi = \text{const} \int_{-\infty}^0 dZ e^{-\mu_f |Z|} \sum_{p=s} n_p(Z) |\mathbf{S}(\phi_p, Z)|, \quad (4)$$

where  $\mu_f$  is the linear absorption coefficient of the MnK $\alpha$  fluorescence radiation in GaAs and  $n_p(Z)$  is the concentration profile of the particular impurity in the (Ga,Mn)As epilayer normalized to 1 ( $p = s, i^{(1)}, i^{(2)}$ ), e.g.,  $n_s=1$  for substitutional Mn occupying all Ga sites. Equation (4) is the basis for numerical simulations; the resulting fluorescence signal  $\Phi$  is convoluted with the angular distributions of the primary beam intensity both in azimuthal direction and in the direction perpendicular to the sample surface. The fluorescence signal for randomly distributed Mn atoms,  $\text{Mn}_r$ , is simulated numerically by averaging the value of  $\Phi$  obtained from Eq. (4) over all values of the phase  $\phi$ . Note that  $\text{Mn}_r$  atoms can represent another phases present in the sample (MnAs for instance), or can be incorporated, e.g., in an amorphous surface oxide layer.

An important advantage of the grazing-incidence geometry is that the penetration depth of the primary x-ray radiation can be sensitively tuned by changing its incidence angle  $\alpha_i$ , as shown in Fig. 3. Slightly below the critical angle  $\alpha_c$  ( $\alpha_c \approx 0.24^\circ$  in GaAs for 10 keV beam energy) the penetration depth is only a few nanometers so that the fluorescence signal stems from Mn atoms in a very thin surface layer. When crossing the critical angle the penetration depth steeply increases and for  $\alpha_i$  only slightly larger than  $\alpha_c$  it exceeds 100 nm which is the thickness of the studied (Ga,Mn)As layer.

Fig. 4 shows the fluorescence signal calculated for substitutional  $\text{Mn}_{\text{Ga}}$ , for interstitial  $\text{Mn}_i^{(1)}$ , and for  $\text{Mn}_r$  positions. Note that for the (001) surface orientation,  $\text{Mn}_i^{(2)}$  have the same lateral position as  $\text{Mn}_{\text{Ga}}$  and, therefore,

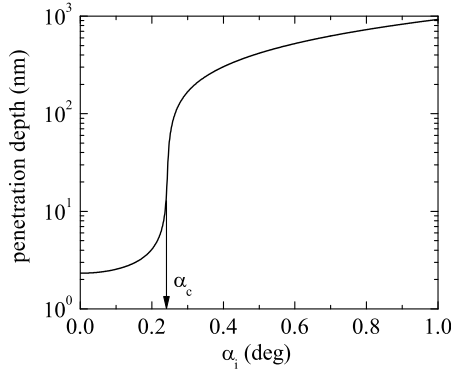


FIG. 3: The dependence of the penetration depth of the primary x-ray beam on the incidence angle  $\alpha_i$  in GaAs calculated the energy of 10 keV;  $\alpha_c$  denotes the critical angle of total external reflection.

these two impurities cannot be distinguished by measuring XSW fluorescence in the grazing incidence geometry. The theoretical fluorescence signal is plotted as a function of the azimuthal deviations  $\delta\eta_i$  of the primary x-ray beam from the diffraction maximum for several incidence angles  $\alpha_i = [0.20, 0.22, 0.24, 0.26, 0.28]$  deg near the critical angle. The calculations were performed for in-plane 400, 220, 200 and 420 diffractions, assuming that the Mn atoms are homogeneously distributed over the whole width of the (Ga,Mn)As layer. The energy of the primary beam considered in the calculations is 10 keV. The theory curves illustrate that substitutional and random positions can be identified mainly from the strong 400 and 220 diffractions while the  $\text{Mn}_i^{(1)}$  positions from the weak 200 or 420 diffractions.

In Fig. 5 we plot the calculated dependence of the fluorescence signal on the incidence angle  $\alpha_i$  far from the diffraction position. Since the signal here is excited by the transmitted wave, its  $\alpha_i$ -dependence is determined only by the penetration depth of the incoming radiation. Indeed, below the critical angle the calculated fluorescence is very weak while it steeply increases for  $\alpha_i > \alpha_c$ . Note that the shape of the curve does not depend on the position of Mn atoms in the unit cell. To illustrate the sensitivity of the  $\alpha_i$ -dependence of the fluorescence on inhomogeneities in the Mn depth profile, two curves are plotted in Fig. 5; the solid line corresponds to a uniform Mn distribution within the whole 100 nm thick (Ga,Mn)As layer, the dashed line was obtained assuming a 10 nm Mn-rich surface layer with a  $10\times$  larger Mn density.

#### IV. RESULTS

We now present and analyze experimental data measured in the four (Ga,Mn)As layers. Since the collected fluorescence data provide a more direct information on Mn positions in the lattice and allow us to study both

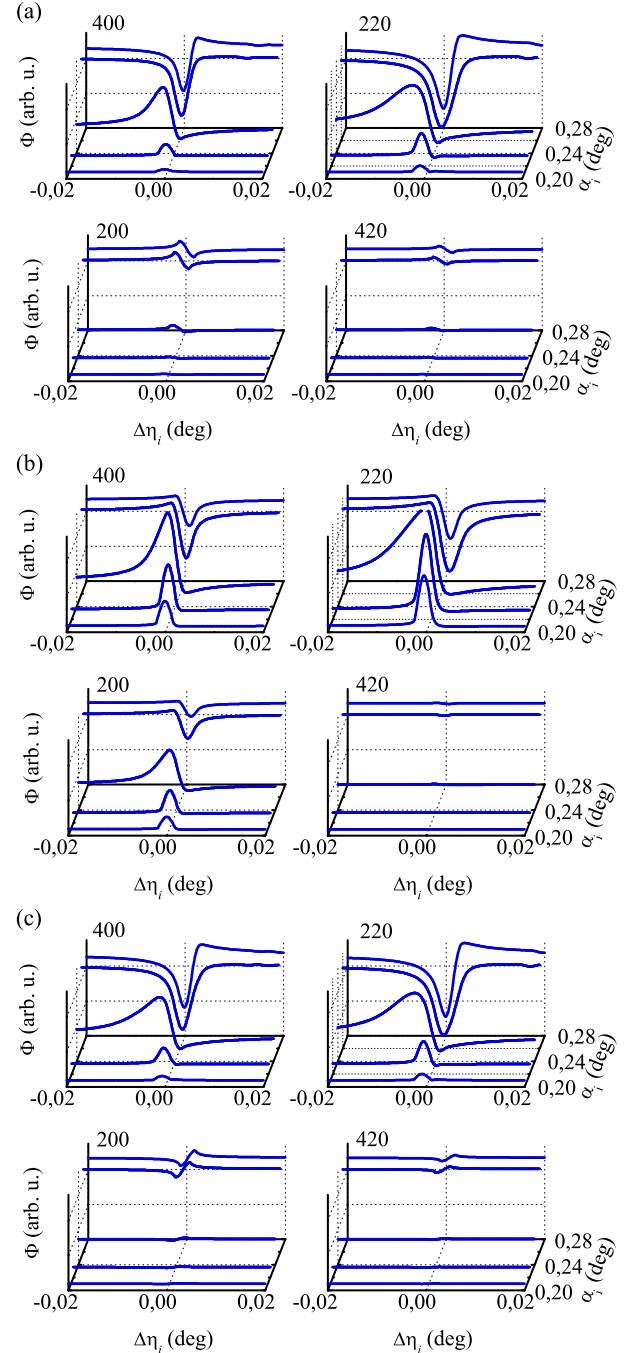


FIG. 4: The MnK $\alpha$  fluorescence intensities calculated for the Mn atoms in substitutional positions (or in  $\text{Mn}_i^{(2)}$ ) (a), in the random positions  $\text{Mn}_r$  (b), and in the  $\text{Mn}_i^{(1)}$  positions (c), in four in-plane diffractions 400, 220, 200 and 420 (surface (001)).

the ordered epilayer part of the (Ga,Mn)As film and the more disordered surface layer we start with this technique. Results of the XSW experiments are also used to make a more detailed interpretation of the XRD measurements of the (Ga,Mn)As epilayer which are presented in the following subsection. As will become clear by the end

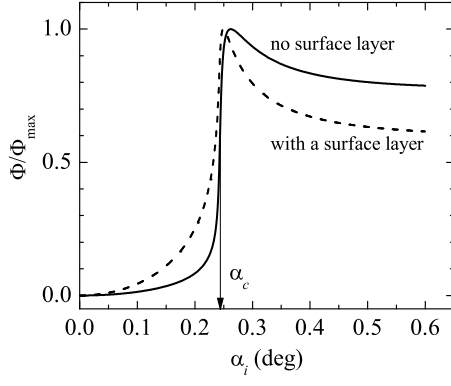


FIG. 5: The dependence of the fluorescence signal on the incidence angle  $\alpha_i$  calculated for the azimuthal direction of the primary beam far from the diffraction position, assuming a homogeneous distribution of Mn atoms (solid line), and a surface layer 10 nm thick, where the Mn density is 10 times larger (dashed line). The curves do not depend on the positions of the Mn atoms in the unit cell and on the diffraction used.  $\alpha_c$  is the critical angle of total external reflection; the curves are normalized to their maxima.

of this section the two techniques, however, are largely complementary and both essential for the conclusions we arrived at in this work.

#### A. X-ray standing-wave fluorescence from Mn atoms

Before resorting to the more elaborate standing-wave experiments, the role of the surface during annealing can be tested by fluorescence measurements without the XSW effect, i.e., for large azimuthal deviations  $\delta\eta_i$  from the diffraction maximum. The comparison of experimental data shown in Fig. 6 with theoretical curves in Fig. 5 clearly indicates the development of a Mn-rich surface layer during the annealing process. The experimental curves could be equally well fitted assuming the thickness of the Mn-rich layer between 2 and 10 nm; the fitted surface density then increases correspondingly to the decrease of the assumed surface layer thickness. This ambiguity partly hinders quantitative interpretation, nevertheless, the Mn-rich surface layer in annealed samples is ubiquitous. As an illustration we give in Tab. I values of the fitted surface Mn density  $N$  relative to the density  $n$  in the homogeneous epilayer beneath the surface layer assuming a fixed Mn-rich layer thickness of 3 nm for all four samples.

The origin of Mn atoms arriving at the surface during annealing and their incorporation in the surface layer is elucidated by the fluorescence measurements in the grazing-incidence XSW geometry. Examples of the measured  $\Phi(\delta\eta_i)$  curves for  $\alpha_i > \alpha_c$  and  $\alpha_i < \alpha_c$  are shown in Figs. 7 and 8, respectively. For the incidence angle  $\alpha_i \approx 0.35^\circ > \alpha_c$  the penetration depth of the primary beam is much larger than 100 nm, i.e., the XSW sig-

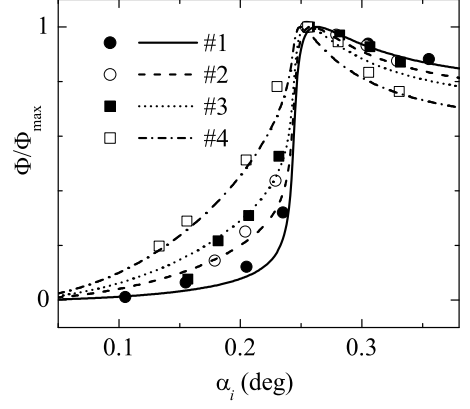


FIG. 6: The fluorescence signal measured for large angular deviations  $\delta\eta_i$  from the diffraction maximum for various incidence angles (points) and its theoretical fit (lines). The curves are normalized to their maximum values.

nal is averaged over the entire layer volume. The XSW curves in Fig. 7 were fitted for all diffractions simultaneously and from the fit we could determine the density  $p_r$  of  $\text{Mn}_r$  relative to the density of the substitutional  $\text{Mn}_{\text{Ga}}$  atoms plus  $\text{Mn}_i^{(2)}$  atoms, i.e.,  $p_r = \bar{n}_r / (\bar{n}_s + \bar{n}_i^{(2)})$ , and the relative density of  $\text{Mn}_i^{(1)}$ ,  $p_i^{(1)} = \bar{n}_i^{(1)} / (\bar{n}_s + \bar{n}_i^{(2)})$ . Because of the large penetration depth of the incidence beam the quantities represent average densities over the entire (Ga,Mn)As layer.

Similar fitting procedure was applied to data measured at  $\alpha_i < \alpha_c$ , shown in Fig. 8. Here the penetration depth of the primary beam is only 3 nm so the fitted densities correspond to a thin surface layer. The  $\text{Mn}_r$  atoms with high surface density were detected even at this small incidence angle, however, the data were not sensitive enough to measure the  $\text{Mn}_i^{(1)}$  impurities. For the fitting we used the values for the relative  $\text{Mn}_i^{(1)}$  densities from the measurements at  $\alpha_i > \alpha_c$  and determined only the relative density  $P_r$  of  $\text{Mn}_r$  in the surface layer.

Results of the XSW experiments are summarized in Tab. I. For convenience we also included in the table partial Mn impurity concentration recalculated relatively to the total combined density of  $\text{Mn}_{\text{Ga}}$ ,  $\text{Mn}_i^{(2)}$ ,  $\text{Mn}_i^{(1)}$ , and  $\text{Mn}_r$ , for both  $\alpha_i < \alpha_c$  and  $\alpha_i > \alpha_c$ . In particular, we show the values of the bulk relative densities

$$q_r = \frac{\bar{n}_r}{\bar{n}} = \frac{p_r}{1 + p_r + p_i^{(1)}}, \quad q_s + q_i^{(2)} = \frac{\bar{n}_s + \bar{n}_i^{(2)}}{\bar{n}} = \frac{1}{1 + p_r + p_i^{(1)}},$$

and the relative density of the  $\text{Mn}_r$  atoms in the surface layer

$$Q_r = \frac{P_r}{1 + P_r + p_i^{(1)}}.$$

From the data in Tab. I we can draw the following conclusions: (i) The number of  $\text{Mn}_r$  atoms systematically increases with annealing time. (ii) Since  $P_r/p_r$  is similar

| sample | $N/n$         | $p_r$           | $p_i^{(1)}$      | $P_r$      | $q_s + q_i^{(2)}$ | $q_r$ | $Q_r$ |
|--------|---------------|-----------------|------------------|------------|-------------------|-------|-------|
| #1     | $1.1 \pm 0.1$ | $0.12 \pm 0.01$ | $0.04 \pm 0.01$  | $2 \pm 1$  | 0.865             | 0.1   | 0.62  |
| #2     | $5 \pm 2$     | $0.22 \pm 0.01$ | $0.025 \pm 0.05$ | $5 \pm 1$  | 0.80              | 0.18  | 0.825 |
| #3     | $12 \pm 3$    | $0.28 \pm 0.05$ | $0.035 \pm 0.01$ | $8 \pm 2$  | 0.76              | 0.21  | 0.88  |
| #4     | $17 \pm 3$    | $0.36 \pm 0.10$ | $0.06 \pm 0.01$  | $15 \pm 4$ | 0.705             | 0.255 | 0.935 |

TABLE I: The parameters obtained from the measured XSW curves.  $N/n$  is the ratio of the total Mn density in the surface layer and the total Mn density  $n = 3.5\%$  in the homogeneous epilayer beneath the surface layer.  $p_r$ ,  $p_i^{(1)}$  are the densities of  $\text{Mn}_r$  and  $\text{Mn}_i^{(1)}$ , respectively, relative to the density of  $\text{Mn}_{\text{Ga}}$  plus  $\text{Mn}_i^{(2)}$  atoms, obtained from the XSW data at  $\alpha_i > \alpha_c$ .  $P_r$  is the relative density of  $\text{Mn}_r$  obtained for  $\alpha_i < \alpha_c$ .  $q_s + q_i^{(2)}$  and  $q_r$  are the recalculated partial concentrations of  $\text{Mn}_{\text{Ga}}$  plus  $\text{Mn}_i^{(2)}$  and of  $\text{Mn}_r$ , respectively, for  $\alpha_i > \alpha_c$ ;  $Q_r$  is the recalculated partial concentration of  $\text{Mn}_r$  for  $\alpha_i < \alpha_c$  (see the text for more details).

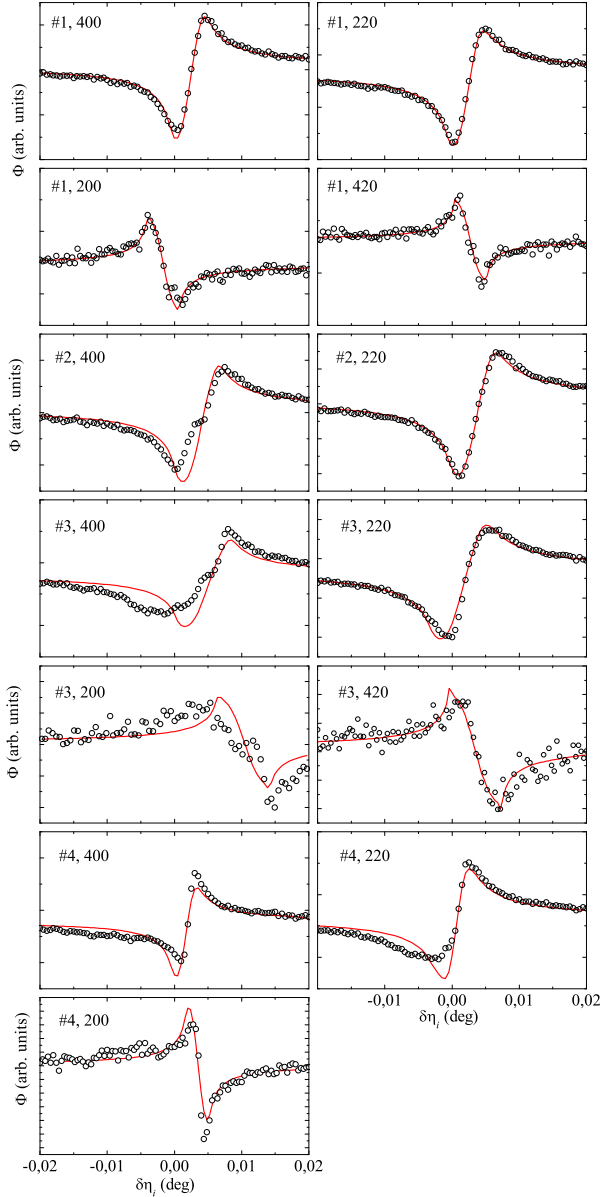


FIG. 7: The XSW scans of samples #1 to #4 measured in various in-plane diffractions for the incidence angle  $\alpha_i \approx 0.35$  deg ( $> \alpha_c$ ) (points) and their theoretical fits (lines).

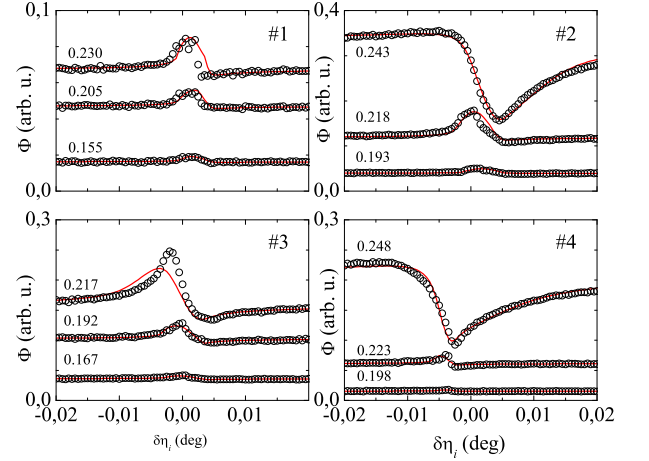


FIG. 8: The XSW scans of samples #1 to #4 measured in the 220 in-plane diffraction for three incidence angle smaller or close to the critical angle  $\alpha_c$  (points) and their theoretical fits (lines). The values of the incidence angle  $\alpha_i$  in deg are indicated above the corresponding curve.

to the ratio between the (Ga,Mn)As layer thickness and the exposed surface layer width in the  $\alpha_i < \alpha_c$  experiment,  $\text{Mn}_r$  atoms are concentrated in the surface layer. This also means a marginal role (if any) of second phases in the (Ga,Mn)As epilayer. (iii) As the  $\text{Mn}_r$  atoms fill the surface, the density of  $\text{Mn}_{\text{Ga}}$  plus  $\text{Mn}_i^{(2)}$  impurities in the (Ga,Mn)As layer decreases. The XRD data discussed in the following subsection show that the density of substitutional  $\text{Mn}_{\text{Ga}}$  atoms remains constant during annealing. We can, therefore, directly link the outdiffusion of interstitial  $\text{Mn}_i^{(2)}$  from the (Ga,Mn)As with the build-up of the  $\text{Mn}_r$ -rich surface layer. Note that we detected only a small density of  $\text{Mn}_i^{(1)}$  impurities and no systematic behavior during annealing can be extracted from the data.

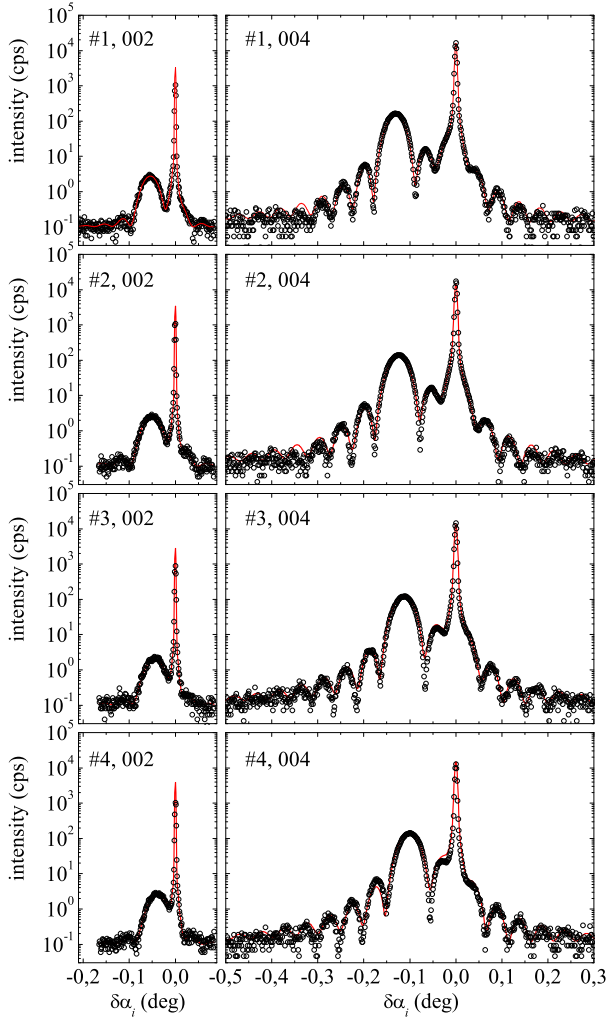


FIG. 9: High-resolution x-ray diffraction curves of samples #1 to #4 in diffractions 002 (left column) and 004 (right column) (points) and their fits by conventional dynamical diffraction theory (lines).

### B. X-ray diffraction from (Ga,Mn)As epilayers

Experimental XRD curves, along with their fits obtained by conventional dynamical diffraction theory, are shown in Fig. 9. The 002 and 004 diffractions were fitted simultaneously. Local distortions of the lattice around  $\text{Mn}_s$  and  $\text{Mn}_i^{(1,2)}$  atoms were neglected in the fitting procedure. The very good correspondence of experimental and theoretical diffraction curves demonstrates good structural quality of the epilayers and homogeneity of the Mn distribution. No measurable Mn concentration gradients were detected across the epilayer.

The epilayer thickness and the total lattice expansion parameter  $\xi$ , defined as  $a = a_0 + \xi$  where  $a_0$  is the GaAs lattice constant and  $a$  is the relaxed lattice parameter of the (Ga,Mn)As epilayer, were obtained independently with error bars smaller than 1%. Since the average structure factor and consequently the heights of the layer max-

ima on the diffraction curves depend on the impurity type, we were able to measure lattice expansion contributions from individual impurities, albeit with smaller accuracy. In particular, we assumed that  $\xi = \xi_s + \xi_i + \xi_a$ , where the subscript "s" stands for substitutional  $\text{Mn}_{\text{Ga}}$ , "i" for interstitial Mn of both types  $\text{Mn}_i^{(1)}$  and  $\text{Mn}_i^{(2)}$ , and we also included antisite  $\text{As}_{\text{Ga}}$  impurities ( $\xi_a$ ). Note that the expansion parameters  $\xi_p$ ,  $p = s, i, a$  and the Vegard's law dilatation coefficients  $\beta_p$  are related as,  $\xi_p = \beta_p n_p$ .

The influence of  $\text{Mn}_i$  atoms on  $\xi$  was not taken into account in our simulations. Other crystallographic phases, where  $\text{Mn}_i$  atoms are incorporated, could affect the mean lattice constant of the epilayer only if they deform the surrounding crystal lattice and give rise to measurable diffuse x-ray scattering. Consistent with the results of XSW experiments, no such effects were detected in the XRD data for the studied (Ga,Mn)As epilayers.

We found that equally good fits could be obtained assuming any value of  $\xi_a$  ranging from 0 to  $5 \times 10^{-3}$  Å. The extracted total expansion  $\xi$ , shown in Tab. II, is independent of the choice of  $\xi_a$  which immediately implies the dependence of the fitted  $\xi_s$  and  $\xi_i$  on  $\xi_a$ . In Tab. II we show expansion parameters obtained for the two limiting values of  $\xi_a$ . Despite the quantitative ambiguities in the values of individual expansion parameters we can safely conclude that the lattice constant decreases during annealing, that the density of  $\text{Mn}_{\text{Ga}}$  atoms remains constant and, consequently, the decrease of the total lattice parameter with annealing time is due to the removal of  $\text{Mn}_i$  impurities from the ordered epilayer part of the (Ga,Mn)As film. (Note that  $\text{As}_{\text{Ga}}$  antisites in GaAs are stable up to  $\sim 450^\circ\text{C}$ .<sup>21</sup>)

Although the XRD and XSW experiments did not allow to separately determine  $\text{Mn}_{\text{Ga}}$  and  $\text{Mn}_i$  partial densities, the p-type character of the (Ga,Mn)As semiconductor and the single acceptor nature of  $\text{Mn}_{\text{Ga}}$  and the double-donor nature of  $\text{Mn}_i$  and of  $\text{As}_{\text{Ga}}$  imply that  $n_s > 2n_i$ . From this and from the expansion parameters in Tab. II we obtain that the dilatation coefficient  $\beta_i$  is at least  $10\times$  larger than  $\beta_s$ . A significantly larger lattice expansion due to  $\text{Mn}_i$  as compared to  $\text{Mn}_{\text{Ga}}$  is consistent with *ab initio* theory predictions.<sup>22,31</sup>

Using the results of XSW measurements and recalling that  $\text{Mn}_i$  are the only unstable impurities during annealing which contribute to  $\xi$  we can also make an estimate for the absolute value of  $\beta_i$ . The measured changes in  $\xi$  after each annealing step and the  $\text{Mn}_i$  expansion coefficient are related as,  $\beta_i = \Delta\xi_i / \Delta n_i$ , where  $\Delta n_i = n[\Delta q_i^{(1)} + \Delta(q_s + q_i^{(2)})]$ . For  $n$  we can take the MBE growth value  $3.5 \pm 0.5\%$ , and the changes of the relative partial concentrations can be read out from Tab I. The value  $\beta_i = 0.4 \pm 0.2$  we arrive at has an appreciable scatter, reminiscent of the current theoretical uncertainty for this coefficient.<sup>22,31</sup> Nevertheless, the experiment and theory are consistent within these error bars.

| sample | $\xi = \sum_{p=s,i,a} \beta_p n_p \text{ (10}^{-3}\text{Å)}$ | $(\beta_s n_s) \text{ (10}^{-3}\text{Å)}$ $(\beta_i n_i) \text{ (10}^{-3}\text{Å)}$ |               | $(\beta_s n_s) \text{ (10}^{-3}\text{Å)}$ $(\beta_i n_i) \text{ (10}^{-3}\text{Å)}$ |               |
|--------|--|---|---------------|---|---------------|
|        |  | for $\xi_a = 0$   |               | for $\xi_a = 5 \times 10^{-3} \text{ Å}$  |               |
| #1     | $10.2 \pm 0.1$   | $1.3 \pm 0.6$   | $8.9 \pm 0.5$ | $0.9 \pm 0.6$   | $4.3 \pm 0.5$ |
| #2     | $9.6 \pm 0.1$  | $1.4 \pm 0.6$   | $8.2 \pm 0.5$ | $0.8 \pm 0.6$   | $4.0 \pm 0.5$ |
| #3     | $8.9 \pm 0.1$  | $1.3 \pm 0.6$   | $7.6 \pm 0.5$ | $0.8 \pm 0.6$   | $3.1 \pm 0.5$ |
| #4     | $8.0 \pm 0.1$  | $1.4 \pm 0.6$   | $6.6 \pm 0.5$ | $0.9 \pm 0.6$   | $2.1 \pm 0.5$ |

TABLE II: Lattice expansion parameters of the (Ga,Mn)As epilayers determined from the XRD measurements.

## V. DISCUSSION

Our experiments confirm the basic picture derived from previous studies of Mn incorporation in (Ga,Mn)As and of the annealing process but the measurements are more direct and provide more detailed information about the structure of the (Ga,Mn)As epilayer and of the layer surface. The XSW measurements clearly indicate the existence of a Mn<sub>r</sub>-rich surface layer. The detailed chemistry of this layer is unknown to us; it could be a surface oxide growing during annealing of (Ga,Mn)As in air, or a very thin MnAs layer.

The small number of Mn<sub>i</sub><sup>(1)</sup> we detected also requires further investigation. In particular, it would be useful to use a XSW geometry in which both Mn<sub>i</sub><sup>(1)</sup> and Mn<sub>i</sub><sup>(2)</sup> can be detected independently. Such a geometry together with calibration measurements on pure Mn crystal should allow for a fully quantitative interpretation of the XSW data. In order to detect Mn<sub>i</sub><sup>(2)</sup> independently of Mn<sub>Ga</sub> atoms, it would be necessary to use a diffraction with a non-zero out-of-plane component of the diffraction vector **h**, since Mn<sub>Ga</sub> and Mn<sub>i</sub><sup>(2)</sup> atoms differ only in their vertical positions. For such a diffraction, the XSW effect can be measured (i) in the case of a very thin (Ga,Mn)As layer or (ii) for a very thick layer. In the former case, the diffraction in substrate can be used for the creation of the standing wave and the (Ga,Mn)As layer has to be very thin so that the vertical misalignment of the Mn atoms (due to the lattice mismatch) with respect to the standing wave pattern is negligible. This condition is fulfilled for the layer thickness

$$T \ll \frac{a_{\text{sub}}}{f}, \quad (5)$$

where  $f = (a_{\text{layer}\perp} - a_{\text{sub}})/a_{\text{sub}}$  is the vertical lattice mismatch of the (Ga,Mn)As epilayer with respect to the GaAs substrate. Since, in our case, the mismatch is of

the order of  $10^{-2}$ , the (Ga,Mn)As layer would have to be much thinner than 50 nm.

In the case (ii), the diffraction in the (Ga,Mn)As epilayer can be used as a source of the standing wave. In order to achieve a measurable XSW effect, the intensities of the primary and diffracted beams must be comparable, i.e., the thickness of the epilayer has to be comparable to the x-ray extinction length (above 1  $\mu\text{m}$ ). Note however, that theoretical analysis of these experiments will be complicated by the fact that the standing wave itself is affected by the presence of Mn atoms.

## VI. CONCLUSIONS

We have studied the structure of epitaxial (Ga,Mn)As layers and their changes during post-growth annealing, using high-resolution x-ray diffraction and grazing-incidence x-ray standing-wave techniques. The layers are formed by a high crystal quality (Ga,Mn)As epilayers covered by a thin Mn-rich layer. We have identified that the excess surface Mn density is due to Mn atoms occupying random positions incommensurate with the host lattice. The increase of the density of random Mn atoms during annealing is correlated with the decrease of interstitial Mn density in the (Ga,Mn)As epilayer.

## Acknowledgment

We acknowledge fruitful collaborations with Dr. Tien-Lin Lee and other members of the beamline ID32 team at ESRF Grenoble, and support from the Ministry of Education of the Czech Republic under Grants No. MSM 0021620834 and LC510, from the Grant Agency of Czech Republic under Grants No. 202/06/0025, 202/05/0575, and 202/04/1519, and from the UK EPSRC under Grant No. GR/S81407/01.

<sup>1</sup> F. Matsukura, H. Ohno, and T. Dietl, in *Handbook of Magnetic Materials*, edited by K. H. J. Buschow (Elsevier, Amsterdam, 2002), vol. 14, p. 1.

<sup>2</sup> T. Jungwirth, J. Sinova, J. Mašek, J. Kučera, and A. H. MacDonald, *Rev. Mod. Phys.* **78**, 809 (2006).

<sup>3</sup> K. M. Yu, W. Walukiewicz, T. Wojtowicz, I. Kuryliszyn,

X. Liu, Y. Sasaki, and J. K. Furdyna, *Phys. Rev. B* **65**, 201303 (2002).

<sup>4</sup> F. Máca and J. Mašek, *Phys. Rev. B* **65**, 235209 (2002).

<sup>5</sup> J. Blinowski and P. Kacman, *Phys. Rev. B* **67**, 121204 (2003).

<sup>6</sup> J. Mašek and F. Máca, *Phys. Rev. B* **69**, 165212 (2003).

- <sup>7</sup> K. W. Edmonds, P. Boguslawski, K. Y. Wang, R. P. Campion, N. R. S. Farley, B. L. Gallagher, C. T. Foxon, M. Sawicki, T. Dietl, M. B. Nardelli, et al., Phys. Rev. Lett. **92**, 037201 (2004).
- <sup>8</sup> T. Jungwirth, K. Y. Wang, J. Mašek, K. W. Edmonds, J. König, J. Sinova, M. Polini, N. A. Goncharuk, A. H. MacDonald, M. Sawicki, et al., Phys. Rev. **B 72**, 165204 (2005).
- <sup>9</sup> T. Jungwirth, J. Mašek, K. Y. Wang, K. W. Edmonds, M. Sawicki, M. Polini, J. Sinova, A. H. MacDonald, R. P. Campion, L. X. Zhao, et al., Phys. Rev. **B 73**, 165205 (2005).
- <sup>10</sup> K. W. Edmonds, K. Y. Wang, R. P. Campion, A. C. Neumann, N. R. S. Farley, B. L. Gallagher, and C. T. Foxon, Appl. Phys. Lett. **81**, 4991 (2002).
- <sup>11</sup> D. Chiba, K. Takamura, F. Matsukura, and H. Ohno, Appl. Phys. Lett. **82**, 3020 (2003).
- <sup>12</sup> K. C. Ku, S. J. Potashnik, R. F. Wang, M. J. Seong, E. Johnston-Halperin, R. C. Meyers, S. H. Chun, A. Mascarenhas, A. C. Gossard, D. D. Awschalom, et al., Appl. Phys. Lett. **82**, 2302 (2003).
- <sup>13</sup> M. B. Stone, K. C. Ku, S. J. Potashnik, B. L. Sheu, N. Samarth, and P. Schiffer, Appl. Phys. Lett. **83**, 4568 (2003).
- <sup>14</sup> Y. Ishiwata, M. Watanabe, R. Eguchi, T. Takeuchi, Y. Harada, A. Chainani, S. Shin, T. Hayashi, Y. Hashimoto, S. Katsumoto, et al., Phys. Rev. **B 65**, 233201 (2002).
- <sup>15</sup> F. Glas, G. Patriarche, L. Largeau, and A. Lemaitre, Phys. Rev. Lett. **93**, 086107 (2004).
- <sup>16</sup> I. Frymark and G. Kowalski, J. Phys. **D 38**, A160 (2005).
- <sup>17</sup> J. Sadowski and J. Z. Domagala, Phys. Rev. **B 69**, 075206 (2004).
- <sup>18</sup> I. Kuryliszyn-Kudelska, J. Z. Domagala, T. Wojtowicz, X. Liu, E. Lusakowska, W. Dobrowolski, and J. K. Furdyna, J. Appl. Phys. **95**, 603 (2004).
- <sup>19</sup> L. X. Zhao, C. R. Staddon, K. Y. Wang, K. W. Edmonds, R. P. Campion, B. L. Gallagher, and C. T. Foxon, Appl. Phys. Lett. **86**, 071902 (2005).
- <sup>20</sup> S. C. Erwin and A. G. Petukhov, Phys. Rev. Lett. **89**, 227201 (2002).
- <sup>21</sup> D. E. Bliss, W. Walukiewicz, J. W. A. III, E. E. Haller, K. T. Chan, and S. Tanigawa, J. Appl. Phys. **71**, 1699 (1992).
- <sup>22</sup> J. Mašek, J. Kudrnovský, and F. Máca, Phys. Rev. **B 67**, 153203 (2003).
- <sup>23</sup> B. J. Kirby, J. A. Borchers, J. J. Rhyne, K. V. O'Donovan, S. G. E. te Velthuis, S. Roy, C. Sanchez-Hanke, T. Wojtowicz, X. Liu, W. L. Lim, et al. (2006), cond-mat/0602182.
- <sup>24</sup> M. Adell, J. Kanski, L. Ilver, V. Stanciu, and P. Svedlindh, Phys. Rev. Lett. **94**, 139701 (2005).
- <sup>25</sup> M. Malfait, J. Vanacken, W. Van Roy, G. Borghs, and V. V. Moshchalkov, Appl. Phys. Lett. **86**, 132501 (2005).
- <sup>26</sup> B. J. Kirby, J. A. Borchers, J. J. Rhyne, K. V. O'Donovan, T. Wojtowicz, X. Liu, Z. Ge, S. Shen, and J. K. Furdyna, Appl. Phys. Lett. **86**, 072506 (2004).
- <sup>27</sup> U. Pietsch, V. Holý, and T. Baumbach, *High-Resolution X-Ray Scattering from Thin Films and Lateral Nanostructures* (Springer Verlag, New York, 2003).
- <sup>28</sup> J. Zegenhagen, Surf. Sci. Reports **18**, 202 (1993).
- <sup>29</sup> I. A. Vartanyants<sup>1</sup> and M. V. Kovalchuk, Rep. Progr. Phys. **64**, 1009 (2001).
- <sup>30</sup> A. Authier, *Dynamical Theory of X-Ray Diffraction* (Oxford Univ. Press, Oxford, 2001).
- <sup>31</sup> J. Mašek and F. Máca, Acta Phys. Pol. **A 108**, 789 (2005), cond-mat/0508760.